JBC ARTICLE

In silico and crystallographic studies identify key structural features of biliverdin IXβ reductase inhibitors having nanomolar potency

Received for publication, January 9, 2018, and in revised form, February 23, 2018 Published, Papers in Press, February 27, 2018, DOI 10.1074/jbc.RA118.001803

Natasha M. Nesbitt[‡1,2], **Xiliang Zheng**[§1], **Zongdong Li**[‡], **José A. Manso**[¶‖], **Wan-Yi Yen**[‡], **Lisa E. Malone**[‡], **Jorge Ripoll-Rozada**[¶‖], **Pedro José Barbosa Pereira**[¶‖], **Timothy J. Mantle**[**], **Jin Wang**[‡‡3], **and Wadie F. Bahou**[‡]

From the Departments of [‡]*Medicine and* [‡‡]*Chemistry and Physics, State University of New York at Stony Brook, Stony Brook, New York 11794-8151, the* [§]*State Key Laboratory of Electroanalytical Chemistry, Changchun Institute of Applied Chemistry, Chinese Academy of Sciences, ChangChun, Jilin 130022, China, the* [¶]*IBMC - Instituto de Biologia Molecular e Celular, Universidade do Porto, 4200-135 Porto, Portugal, the* [‖]*i3S - Instituto de Investigação e Inovação em Saúde, Universidade do Porto, 4200-135 Porto, Portugal, and the* [**]*Department of Biochemistry, Trinity College, Dublin 2, Ireland*

Edited by Wolfgang Peti

Heme cytotoxicity is minimized by a two-step catabolic reaction that generates biliverdin (BV) and bilirubin (BR) tetrapyrroles. The second step is regulated by two non-redundant biliverdin reductases (IXα (BLVRA) and IXβ (BLVRB)), which retain isomeric specificity and NAD(P)H-dependent redox coupling linked to BR's antioxidant function. Defective BLVRB enzymatic activity with antioxidant mishandling has been implicated in metabolic consequences of hematopoietic lineage fate and enhanced platelet counts in humans. We now outline an integrated platform of *in silico* and crystallographic studies for the identification of an initial class of compounds inhibiting BLVRB with potencies in the nanomolar range. We found that the most potent BLVRB inhibitors contain a tricyclic hydrocarbon core structure similar to the isoalloxazine ring of flavin mononucleotide and that both xanthene- and acridine-based compounds inhibit BLVRB's flavin and dichlorophenolindophenol (DCPIP) reductase functions. Crystallographic studies of ternary complexes with BLVRB–NADP$^+$–xanthene-based compounds confirmed inhibitor binding adjacent to the cofactor nicotinamide and interactions with the Ser-111 side chain. This residue previously has been identified as critical for maintaining the enzymatic active site and cellular reductase functions in hematopoietic cells. Both acridine- and xanthene-based compounds caused selective and concentration-dependent loss of redox coupling in BLVRB-overexpressing promyelocytic HL-60 cells. These results provide promising chemical scaffolds for the development of enhanced BLVRB inhibitors and identify chemical probes to better dissect the role of biliverdins, alternative substrates, and BLVRB function in physiologically relevant cellular contexts.

Heme proteins are found in nearly all phyla, and are degraded by oxidative cleavage to release iron and initiate derivatization of the tetrapyrrole backbone for downstream metabolic usage or disposal. The vast majority of heme oxygenases studied to date utilize cytochrome P450 reductase or reduced ferredoxin as an electron source (1), and sequentially cleave heme to biliverdin (BV),[4] which is then reduced to bilirubin (BR) (2). BR is an antioxidant (3), has been associated with lower cardiovascular risk (4–6), and is implicated in a putative antioxidant BV/BR redox cycle regulated by biliverdin reductase (7). Although heme cleavage would be expected at any of the four *meso* bridge carbons (yielding BV isomers IXα, IXβ, IXγ, and IXδ), mammalian BVs are primarily generated by regioselective cleavage at the α-*meso* carbon (BV IXα), with limited identification of BV (or BR) IXβ, IXγ, or IXδ in adults. In contrast, isomeric composition appears distinct in the fetus where BR IXβ is the

This work was supported in part by National Institutes of Health Grants HL091939 (to W. F. B.) and HL129545 (to N. M. N.), New York State Stem Cell Foundation Grant C026716 (to W. F. B.), National Natural Science Foundation of China Grant 91430217, MOST Grants 2016YFA0203200 and 2013YQ170585 (to X. L. Z. and J. W.), National Science Foundation Grant PHY-76066 (to J. W.), Portuguese funds through Fundação para a Ciência e a Tecnologia postdoctoral fellowship SFRH/BPD/108004/2015 (to J. R.-R.) and project "Institute for Research and Innovation in Health Sciences" Grant POCI-01–0145-FEDER-007274, co-funded by the European Regional Development Fund (FEDER) through the COMPETE 2020-Operational Programme for Competitiveness and Internationalization (POCI), PORTUGAL 2020, the "Structured program on bioengineered therapies for infectious diseases and tissue regeneration" Grant Norte-01-0145-FEDER-000012, supported by Norte Portugal Regional Operational Programme (NORTE 2020), under the PORTUGAL 2020 Partnership Agreement through FEDER. The authors declare that they have no conflicts of interest with the contents of this article. The content is solely the responsibility of the authors and does not necessarily represent the official views of the National Institutes of Health.

This article contains Tables S1–S5 and Figs. S1–S3.

The atomic coordinates and structure factors (codes 5OOG and 5OOH) have been deposited in the Protein Data Bank (http://wwpdb.org/).

The diffraction data (http://dx.doi.org/10.15785/SBGRID/484, http://dx.doi.org/10.15785/SBGRID/485, http://dx.doi.org/10.15785/SBGRID/486, http://dx.doi.org/10.15785/SBGRID/487) were deposited with the SBGrid Data Bank (https://data.sbgrid.org/).

[1] Both authors contributed equally to this work.

[2] To whom correspondence may be addressed. Tel.: 631-216-7425; E-mail: natasha.nesbitt@stonybrook.edu.

[3] To whom correspondence may be addressed. Tel.: 631-632-1185; E-mail: jin.wang.1@stonybrook.edu.

[4] The abbreviations used are: BV, biliverdin; BLVRB, biliverdin IXβ reductase; BR, bilirubin; FMN, flavin mononucleotide; NADPH, reduced nicotinamide adenine dinucleotide phosphate; NADP$^+$, oxidized nicotinamide adenine dinucleotide phosphate; FR, flavin reductase; DCPIP, 2,6-dichloroindophenol; ISR, intrinsic specificity ratio; r.m.s. deviation, root mean square deviation; 2D-VS, two-dimensional virtual screen; GST, glutathione *S*-transferase; BBB, blood-brain barrier; PDB, Protein Data Bank; Lv, lentivirus.

predominant rubin in neonatal bile (8), although the mechanism for BV IXβ generation remains enigmatic.

Two monomeric pyridine nucleotide oxidoreductases (biliverdin reductases) catalyze the reduction of the four isomers to generate the corresponding bilirubins. Both biliverdin reductases are members of the short chain dehydrogenase/reductase protein family (9) but retain distinct specificities for BV reduction. In humans, biliverdin reductase IXα (BLVRA) (10–12) effectively reduces BV IXα with less efficient utilization of BV IXβ, IXγ, or IXδ (13). In contrast, biliverdin IXβ reductase (BLVRB) is promiscuous (14, 15), catalyzing the NAD(P)H-dependent reduction of non-IXα biliverdin isomers (IXβ, IXγ, and IXδ) (16), and several flavins, including flavin mononucleotide (FMN) (17), pyrroloquinoline quinone (18), dichlorophenolindophenol (DCPIP), and ferric ion (Fig. 1*a*) (18). A single dinucleotide-binding domain accommodates both NADPH (or NADH) and substrate(s) within the verdin/flavin (V/F) binding pocket, with no evidence to date for structural or preferred partitioning for either substrate. BLVRB catalysis likely includes both stepwise (19) and concerted (20) mechanisms, with progressive support for a compulsory two-step mechanism initiated by NADPH binding (19–21). Protonation of the pyrrolic nitrogen is the likely first step followed by hydride transfer from the nicotinamide for bilirubin formation; bulk solvent is the presumed proton source with no evidence to date for alternative source(s) based on crystallographic structure and mutagenesis studies (9, 19).

BLVRB is best characterized as a flavin reductase; however, its physiological function(s) and target(s) remain elusive because of its lack of activity toward the predominant BV IXα isomer found in adults (22). It has been speculated that pyrroloquinoline quinone, which has been found in human milk (23), as well as human organs, plasma, and urine (24), may function as a physiological BLVRB substrate due to the affinity of the enzyme for this compound (25), but this has yet to be confirmed. Interestingly, recent data applying a genetic screen in humans have identified a BLVRB loss-of-function redox mutation (BLVRB^{S111L}) that unmasks a fundamentally important mechanism linking heme degradation to the development of exaggerated thrombopoiesis (platelet production) (26). This mutation affects both flavin and biliverdin coupling, and subsequent experimental and thermodynamic studies provided the foundation for the "encounter" and "equilibrium" states of the binary BLVRB–NADP$^+$ complex, and the critical role of the active site Ser-111 in maintaining enzymatic function and thermodynamic stability mediated by the hydrogen-bonded network (27). We have now extended these data by integrating molecular modeling and crystallographic studies to identify an initial class of BLVRB small molecule inhibitors displaying nanomolar activity. *In vitro* assays using cell-based models establish that BLVRB inhibitors display selective effects on oxidation–reduction (redox) coupling. These data identify critical interactions regulating BLVRB enzymatic function, and outline the initial development of BLVRB inhibitors that can be utilized to probe metabolic and cellular effects of BLVRB function.

Results

We utilized two parallel approaches to identify BLVRB inhibitors (Fig. 1*b*), applying both structural similarity and computational approaches for identification of six inhibitors with enhanced potency in comparison to lumichrome, an inhibitor of BLVRB flavin reductase (FR) activity (17) (Table 1).

Halogenated xanthene-based dyes inhibit BLVRB

A manual search was conducted to identify individual compounds that chemically resembled the BLVRB substrate FMN, ranking them according to availability and solubility in aqueous solutions. Among the identified ligand candidates were xanthene-based dyes and acridine-containing compounds (Table 1 and Fig. S1). Measurement of BLVRB FR activity in the presence of these compounds established that halogenated xanthene dyes functioned as potent inhibitors of BLVRB with IC_{50} values of 0.70 ± 0.36 μM for phloxine B and 0.41 ± 0.09 μM for erythrosin extra bluish. The parent compound, xanthene, displayed low activity against BLVRB confirming that this core structure alone is not sufficient for enzyme inhibition. Both phloxine B and erythrosin extra bluish are poor BLVRA inhibitors, demonstrating 77 ± 3 and 89 ± 2% enzyme activity, respectively, at 10 μM of either compound. These compounds will exhibit IC_{50} values for BLVRA well above concentrations required for BLVRB inhibition.

To explore whether phloxine B and erythrosin extra bluish could inhibit BLVRB using an alternate substrate, compounds were assayed in the presence of the BLVRB substrate DCPIP (28) to determine their effect on its DCPIP reductase activity. Both dyes were shown to inhibit BLVRB activity when DCPIP was used as the substrate ($IC_{50,phloxineB}$ = 1.1 ± 0.1 μM, $IC_{50,erythrosin}$ = 0.22 ± 0.02 μM). This observation indicated that although these compounds are structurally similar to FMN, their inhibitory capabilities are not limited to this substrate.

Two-dimensional virtual screening (2D-VS) hit identification and validation

Phloxine B and erythrosin extra bluish are used as reagents for biological staining, prompting the application of molecular modeling for expanded compound identification; a 2D-VS was modified to incorporate the intrinsic specificity ratio (ISR) as a parameter for ranking hit compounds. In addition to the traditional binding affinity parameter, ISR allows for the discrimination of native binding modes of a protein and its ligand from non-native binding modes (29). Ligands with high ISR scores are predicted to have enhanced selectivity for the protein. We initiated the 2D-VS by re-docking lumichrome into the ligand-binding site of the BLVRB–NADP$^+$–lumichrome crystal structure (PDB entry 1HE5 (22)). The root mean square deviation (r.m.s. deviation) for the ligand between the modeled and experimental lumichrome complex structures was 1.15 Å, thus validating the model. This structure was then used as the template for a 2D-VS against the NCI Diversity Set IV database (Developmental Therapeutics Program), which contains ~1,600 structurally diverse compounds covering the broad chemical space of ~140,000 compounds. This screen led to the identification of 10 compounds that were predicted to have

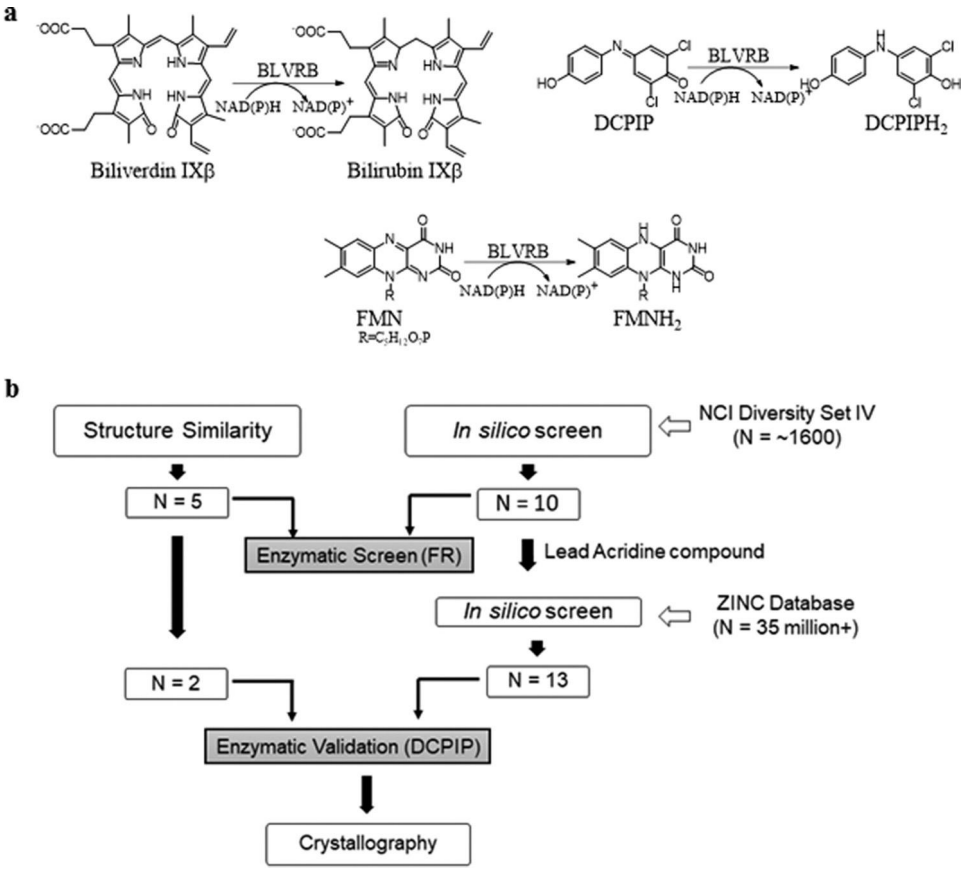

Figure 1. Reactions catalyzed by BLVRB (*a*) and workflow for identifying BLVRB inhibitors (*b*).

enhanced selectivity for BLVRB (Table 1 and Table S2 and Fig. S1), nine of which were soluble and tested for their ability to inhibit BLVRB FR activity. Seven of the identified compounds displayed modest activity (<65%) toward BLVRB, whereas one compound (NSC130813) inhibited >90% of the enzymatic activity (Table S2). As demonstrated using phloxine B and erythrosin extra bluish, NSC130813 inhibited BLVRB enzymatic activity when DCPIP was used as the substrate, displaying activity comparable with that observed using the FR assay (IC_{50} = 30 ± 5 μM).

Expansion of BLVRB inhibitor library

A focused or close analog library was built using similarity and pharmacophore search methods to identify compounds within the ZINC database (30) encompassing scaffolds similar to NSC130813. These *in silico* screens led to the identification of nearly 20,000 "similar" compounds that were further filtered to eliminate non-drug-like compounds (31). Iterative computational studies identified 13 additional compounds based on ISR and predicted affinity, nine of which were commercially available and tested for their ability to inhibit enzymatic activity. ZINC4366439 (NSC12516) was identified as the most potent inhibitor within this second group of compounds with activity toward BLVRB comparable with that of NSC130813. ZINC0977089, ZINC27528243, ZINC21093196, ZINC0977107, and PH006888 contain acridine (or similar polycyclic aromatic) core structures, but have different substitution patterns on their core and/or aniline moieties, and displayed modest (or no) activity toward BLVRB (Table 1 and Fig. S3). Similarly, ZINC71767097 and ZINC71767103, which contain similar substitution patterns on their aniline moieties but have quinolone core structures, displayed minimal activity toward BLVRB (Table S3). These observations indicate that within this group of inhibitors both the acridine and aniline moieties are important for inhibiting BLVRB.

Proposed mode of binding of active inhibitors

Binding modes for top inhibitors were predicted using the AutoDock (32) package (Fig. 2). All four compounds identified from the 2D-VS are located within the substrate-binding site, adjacent to the nicotinamide moiety of the $NADP^+$ cofactor (Fig. 2, *top panel*). As previously described for structures of BLVRB complexed with substrates and inhibitors (22), these compounds are predicted to bind primarily through hydrophobic interactions with the protein. NSC130813 and NSC12516 are docked such that their hydrophobic acridine moieties adopt similar conformations by projecting into the hydrophobic subpocket composed of Gly-76, Ser-111, and Leu-125 (Fig. 2, *middle panel*). The hydroxyl groups located on the phenyl moiety of NSC130813 and NSC12516 form hydrogen bonds (about 2.8 Å) with the main chain nitrogen of Arg-78 and Thr-77 (Fig. 2, *a* and *b*). Different from the interactions of NSC130813 and NSC12516, the acridine nitrogen of PH001924 is predicted to form a hydrogen bond (about 3.2 Å) with the oxygen atom of Ser-111 (Fig. 2*d*). Additionally, its chloro group interacts with the main chain oxygen atom of Thr-129. PH006888 displays a

Small molecule inhibitors of BLVRB

Table 1
Properties of top BLVRB inhibitors

Compound	ID	Predicted Affinity (kcal/mol)	Specificity (ISR)†	IC_{50} (μM)§
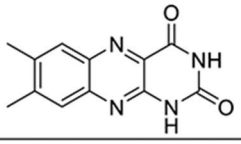	Lumichrome	-5.81	0.87	158 ± 37
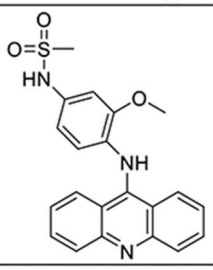	PH006888	-9.88	2.32	89 ± 16
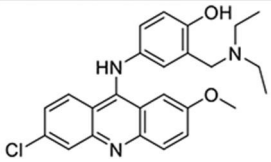	PH001924	-10.12	1.89	36 ± 13
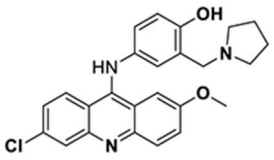	ZINC4366439/ NSC12516	-10.58	3.03	34 ± 6
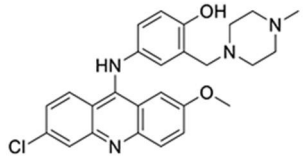	NSC130813	-11.61	3.21	25 ± 5
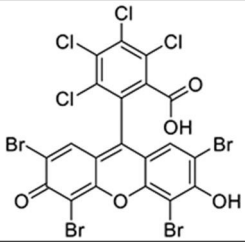	Phloxine B	-8.70	3.28	0.7 ± 0.36
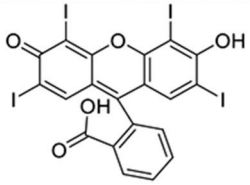	Erythrosin extra bluish	-9.81	1.86	0.41 ± 0.09

† ISR (Intrinsic specificity ratio).
§ Flavin reductase IC_{50} presented as mean ± S.D. of the fit of the experiment run in duplicate.

different binding mode with its acridine moiety being rotated and the acridine nitrogen forming a hydrogen bond with the nitrogen of His-153 (2.82 Å) (Fig. 2*c*). Additionally, the methane sulfonic acid moiety of PH006888 forms two hydrogen bonds (~2.60 Å) with the $NADP^+$ cofactor and the ND1 nitrogen of Thr-77.

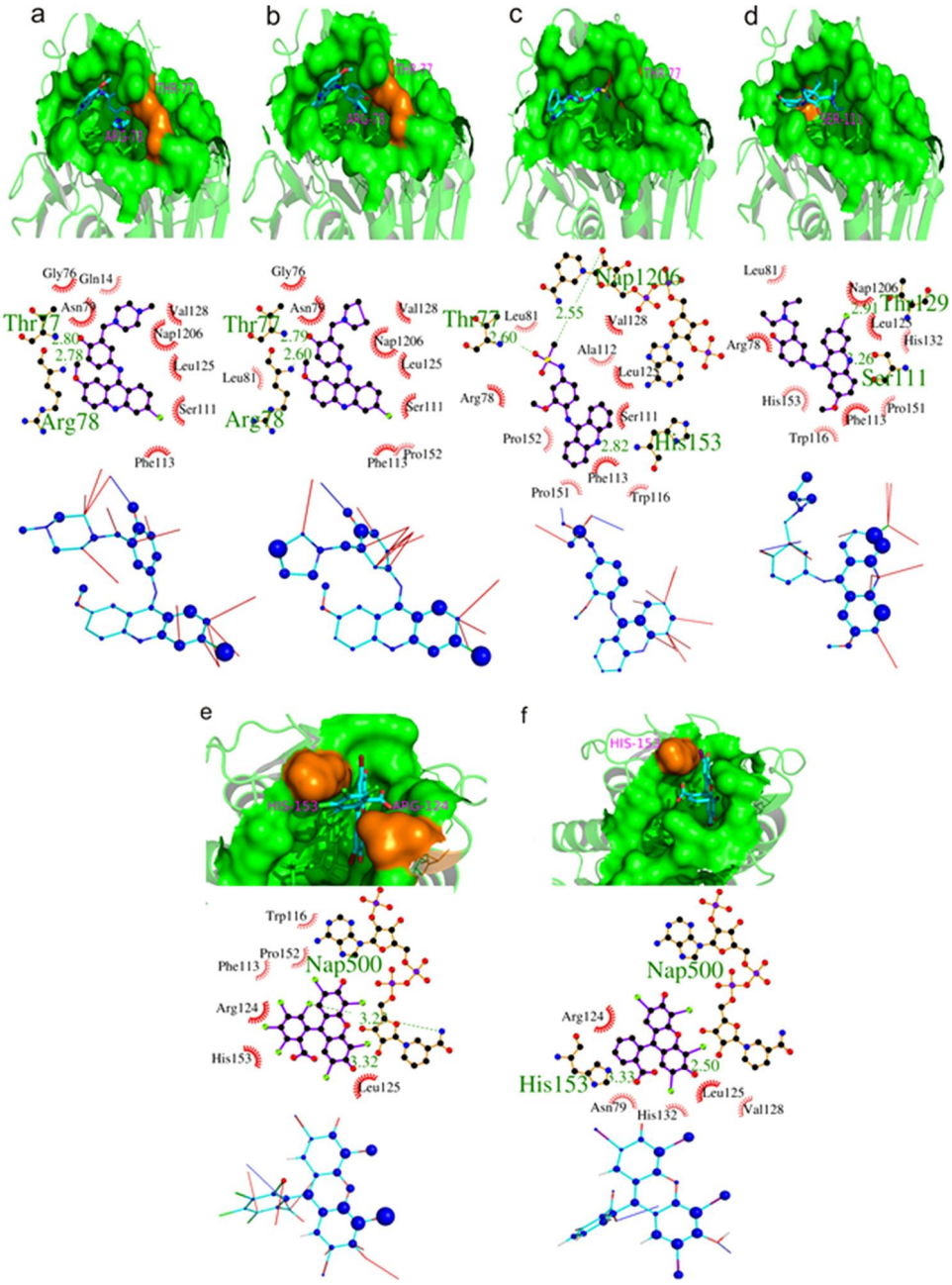

Figure 2. Predicted binding modes of inhibitors. *Top panel*: the hit compounds (*a*) NSC130813, (*b*) NSC12516, (*c*) PH006888, (*d*) PH001924, (*e*) phloxine B, and (*f*) erythrosin extra bluish. The inhibitor (*cyan*) and $NADP^+$ (*green*) are shown in ball-and-stick representation. Residues predicted to be involved in hydrogen bonding are highlighted in *orange*. *Middle panel*: potential enzyme–ligand interactions. The inhibitor (*purple*) and residues predicted to be involved in hydrogen bond interactions (*orange*) are shown in ball-and-stick representation. Hydrogen bonds are indicated by *green dotted lines*, whereas the spoked arcs represent protein residues making non-bonded contacts with the inhibitor. *Bottom panel*: pair potential analysis results for the six ligands. *Blue spheres* indicate "good" pair potential per-atom score with the size of the sphere reflecting the strength of the interaction (*i.e.* the larger the sphere the more attractive the interaction). *Blue* and *red lines* represent good and bad contacts with binding site residues, respectively. Residues within the binding site are not shown for the sake of clarity.

Favorable and unfavorable interactions between BLVRB and inhibitors were identified based on pair potential analyses (Fig. 2, *bottom panel*). The phenyl moiety of NSC130813 and NSC12516 is predicted to make similar contributions (*e.g.* attractive interactions) with BLVRB (Fig. 2, *a* and *b*). In contrast, the acridine moiety of NSC130813 and NSC12516 interacts more favorably through hydrophobic interactions, whereas the same fragment of PH006888 and PH001924 results in less favorable contacts (*e.g.* repulsive interactions; *red lines* in Fig. 2*c* and 2*d*) and fewer contributions (*smaller blue spheres*). These differences account for the lower binding affinity of PH006888 and PH001924 predicted from docking calculations (Table 1). Pair potential analysis predicts that PH006888 is a weak inhibitor of BLVRB due to the large number of unfavorable contacts with the protein.

We assessed the ability of AutoDock (32) to accurately dock phloxine B and erythrosin extra bluish into the ligand-binding site of the BLVRB–$NADP^+$–xanthene-based inhibitor complex

(Fig. 2, *e* and *f*). The r.m.s. deviation for the ligand between the modeled and experimental complex structure (see below) was 0.47 and 1.67 Å (heavy atoms) for phloxine B and erythrosin extra bluish, respectively. Of note, molecular docking studies were performed in the absence of water molecules. Hydrogen bonds between the carbonyl oxygen of phloxine B and erythrosin extra bluish and hydroxyl oxygen O2D from the ribose of $NADP^+$ are formed with an r.m.s. deviation of 3.32 and 2.50 Å, respectively. Additionally, our model predicts that these compounds will bind to BLVRB primarily through hydrophobic interactions. Phloxine B is predicted to establish contacts with Phe-113, Trp-116, Arg-124, Leu-125, Pro-152, and His-153 of BLVRB (Fig. 2*e*, *middle panel*). The chlorine atom of the tetrachlorobenzoate group of phloxine B is predicted to form a hydrogen bond (3.23 Å) with the nitrogen of the carboxamide moiety of the nicotinamide ring of $NADP^+$. The binding pocket for erythrosin extra bluish is predicted to be composed of Asn-79, Arg-124 Leu-125, Val-128, His-132, and His-153 (Fig. 2*f*, *middle panel*). The carboxylate group of the benzoate moiety of erythrosin extra bluish is predicted to form a hydrogen bond (3.33 Å) with the side chain of His-153. As expected, based on their inhibitory activity, both phloxine B and erythrosin extra bluish are predicted to make several favorable interactions with BLVRB (Fig. 2, *e* and *f*, *bottom panel*).

BLVRB inhibitors display non-competitive inhibition toward FMN

Previous studies conducted to elucidate the inhibitory properties of lumichrome showed that this compound is a competitive inhibitor of FMN (17). To investigate the mode of inhibition by erythrosine extra bluish, phloxine B, and NSC130813 we assayed BLVRB using FMN as the variable substrate in the presence of various concentrations of each inhibitor. All three compounds displayed non-competitive inhibition with inhibition constants (K_i) of 0.70 ± 0.032, 1.8 ± 0.096, and 25.1 ± 2.4 μM for erythrosin extra bluish, phloxine B, and NSC130813, respectively (Fig. 3).

Model validation using X-ray crystallography

Model validation for the BLVRB–$NADP^+$–NSC130813 complex was not solvable because of low aqueous solubility of the ligand, although crystal structures of the xanthene-based inhibitors erythrosin extra bluish and phloxine B were determined at 1.33- and 1.20-Å resolution, respectively. The overall structures of phloxine B-bound and erythrosin-bound BLVRB are almost identical to that of ligand-free BLVRB (PDB entry 1HDO (22)), with a r.m.s. deviation of 0.13 and 0.16 Å (204 aligned Cα atoms) for phloxine B-bound and erythrosin-bound BLVRB, respectively. Electron density for the halogenated xanthene moiety of phloxine B was clear in the molecular replacement maps and allowed the straightforward placement of the ligand (Fig. 4*a*). The tetrachlorobenzoate group of phloxine B is disordered and could not be modeled in the electron density maps. The strong anomalous difference peaks observed for the BLVRB–erythrosin extra bluish complex allowed pinpointing the positions of the iodine atoms of the ligand and further facilitated its placement in the electron density maps (Fig. 4*b*). Both substrates are found in the ample binding site of BLVRB, which

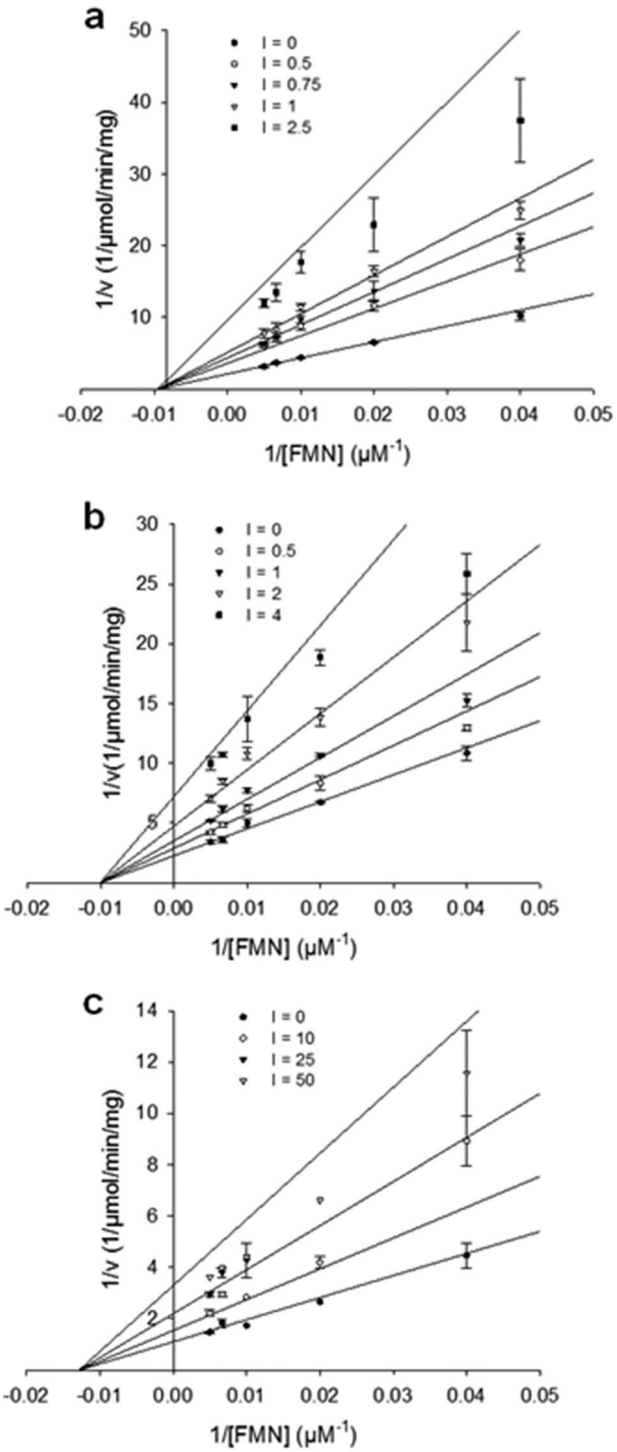

Figure 3. Lineweaver-Burk plots for inhibition of FR activity. *a*, erythrosin extra bluish; *b*, phloxine B; and *c*, NSC130813. *Insets* correspond to concentrations of inhibitor expressed in micromolar. All three inhibitors display non-competitive inhibition with respect to FMN with inhibition constants of 0.70 ± 0.032, 1.8 ± 0.096, and 25.1 ± 2.4 μM for erythrosin extra bluish, phloxine B, and NSC130813, respectively. Data points represent the mean ± S.E. of at least two measurements.

is adjacent to the nicotinamide moiety of the $NADP^+$ cofactor and is bordered by flexible loops 80, 120, and the N-terminal half of helix αE (Fig. 4). Both phloxine B and erythrosin extra bluish bind to BLVRB in a way resembling that described for FMN and lumichrome (22), where a single hydrogen bond is

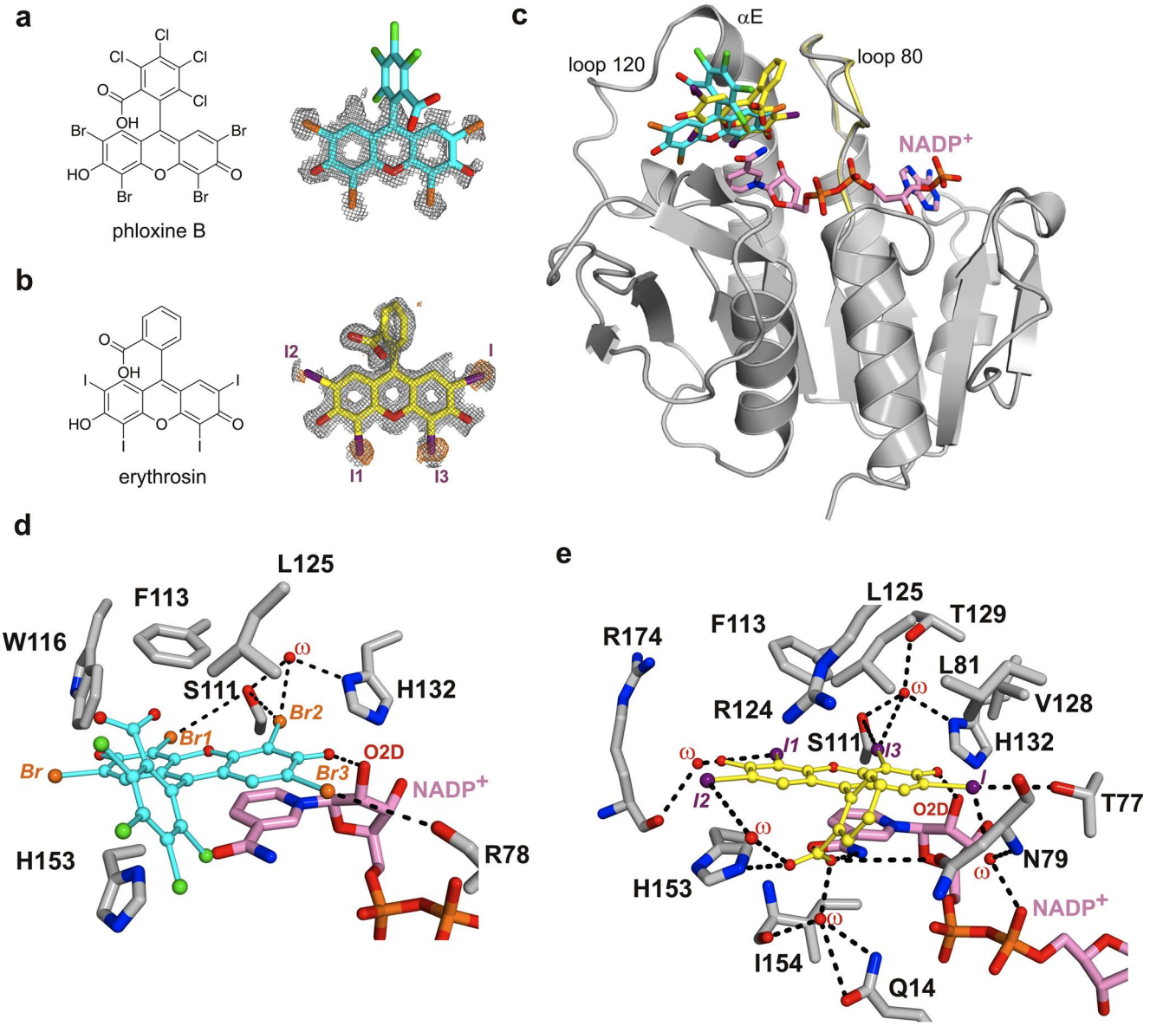

Figure 4. Crystal structures of BLVRB in complex with the xanthene-based dyes phloxine B and erythrosin extra bluish. *a,* the electron density map ($2mF_o - DF_c$ contoured at 1.0 σ) for the halogenated xanthene moiety of phloxine B is shown as a *gray mesh* (*right*). Phloxine B is represented as sticks with oxygen atoms in *red*, chlorine in *green*, bromine in *orange*, and carbon in *cyan*. The structural formula of phloxine B is shown to the *left*. *b,* The electron density ($2m F_o - DF_c$ contoured at 1.0 σ) and anomalous difference (contoured at 3.0 σ) maps for erythrosin extra bluish are shown as *gray* and *orange meshes*, respectively (*right*). The anomalous difference peaks unambiguously indicate the position of the iodine atoms. Erythrosin extra bluish is represented as *sticks* with oxygen atoms in *red*, iodine in *purple,* and carbon in *yellow*. The structural formula of erythrosin extra bluish is shown to the *left*. *c,* ribbon representation of the overlay between the structures of BLVRB in complex with phloxine B and erythrosin extra bluish. The two inhibitors and $NADP^+$ cofactor are represented as sticks (same atom color-coding as in *a* and *b*, except for carbon and phosphorous atoms of $NADP^+$, which are *pink* and *orange*, respectively) with loop 80 of the BLVRB–erythrosin complex shown in *yellow* to highlight the structural differences between the two complexes. Structural elements lining the ligand-binding site and the $NADP^+$ cofactor are labeled. *d* and *e,* interactions of phloxine B and erythrosin extra bluish with the active site of BLVRB. Inhibitors are shown as ball-and-stick models colored as in *a* and *b*. Relevant amino acids and $NADP^+$ are represented as *sticks*, with nitrogen atoms in *blue*, oxygen in *red*, phosphorous in *orange*, and carbon in *gray* (BLVRB) or *pink* ($NADP^+$). Water molecules are represented as *red spheres*. *Black dashed lines* indicate potential polar interactions.

formed between a carbonyl oxygen of the ligand and hydroxyl oxygen O2D from the ribose of the $NADP^+$ cofactor (Figs. 4 and 5*a*). This interaction is preserved in phloxine B and erythrosin extra bluish, involving the equivalent oxygen of each ligand.

Similar to FMN and lumichrome, besides the stacking interaction with the nicotinamide moiety of $NADP^+$, several hydrophobic contacts are established between BLVRB and phloxine B (with the side chains of Phe-113, Trp-116, Leu-125, and His-153) or erythrosin (with the main chain of Asn-79 and the side chains of Leu-81, Phe-113, Arg-124, Leu-125, Val-128, and His-153) (Fig. 4, *d* and *e*). However, whereas the isoalloxazine ring system of FMN and alloxazine ring system of lumichrome are almost perfectly coincident in their complexes with BLVRB (PDB entries 1HE4 and 1HE5 (22)), the xanthone moieties of phloxine B and erythrosin extra bluish deviate significantly from this position (Fig. 5*b*). Although the planes of the isoalloxazine and xanthone moieties are coincident, rotation of

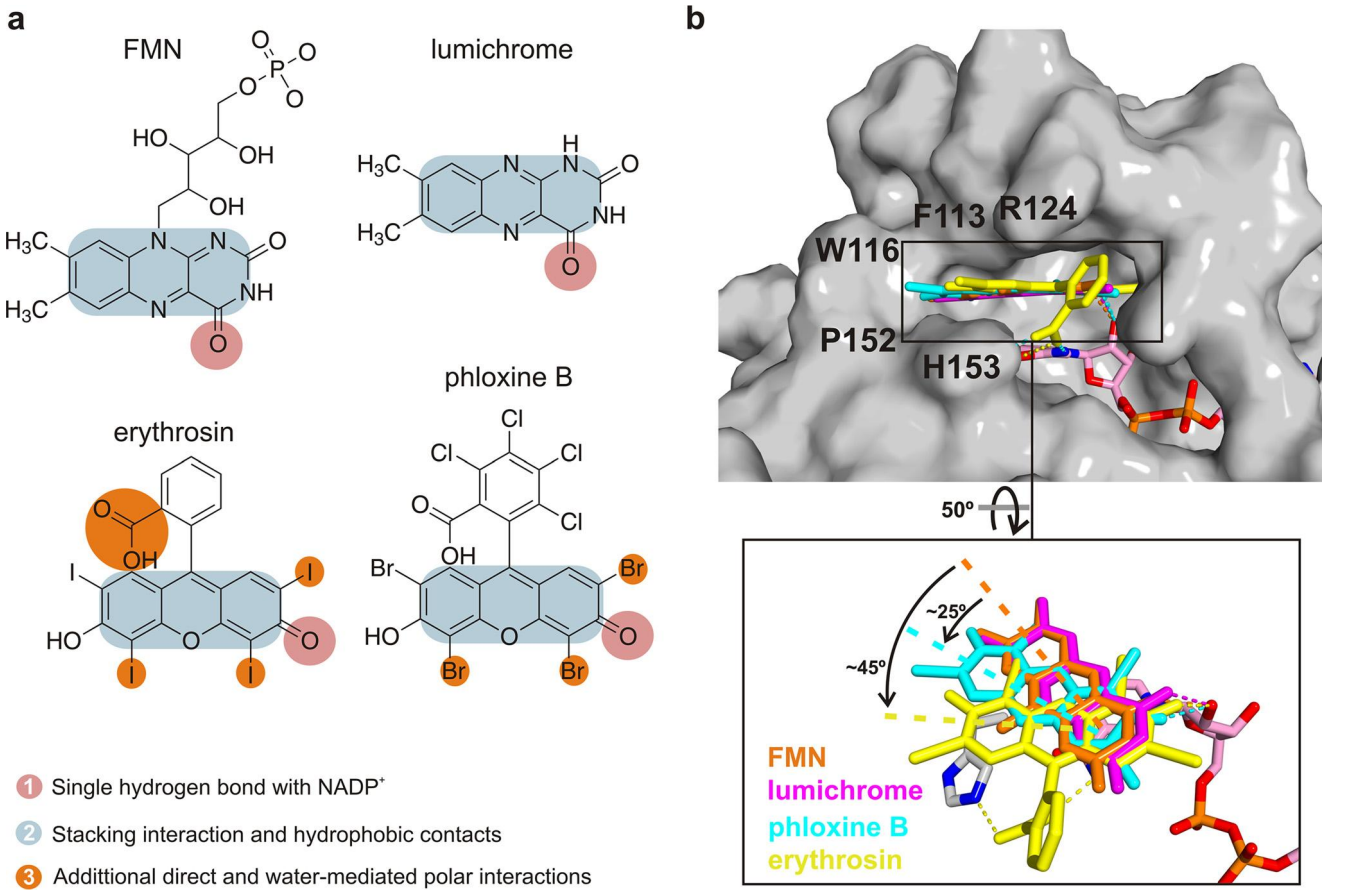

Figure 5. Ligand-binding modes in BLVRB ternary complexes. *a*, schematic representation of the different types of interactions with BLVRB, mapped on the structural formulae of the ligands. *b*, binding modes of FMN (*orange*), lumichrome (*purple*), erythrosin extra bluish (*yellow*), and phloxine B (*cyan*) to BLVRB (solid surface with $NADP^+$ as sticks, with the same color scheme as in Fig. 4*c*; *top*) and close-up view of the isoalloxazine and xanthone moieties of the ligands upon 50° rotation around *x* (*bottom*). The xanthone moieties of phloxine B and erythrosin extra bluish are rotated 25 and 45 degrees relative to FMN, respectively, around an axis perpendicular to the plane of the rings.

the latter around an axis perpendicular to the plane of the ring sitting deeper in the active site of BLVRB, originates a deviation of 25 degrees for phloxine B and 45 degrees for erythrosin extra bluish (Fig. 5*b*). In consequence, phloxine B and erythrosin extra bluish bind less deeply than FMN or lumichrome in the active site of BLVRB, and phloxine O1 and erythrosin O (equivalent to N5 in FMN and lumichrome) are displaced 1.7 or 2.4 Å away from the back wall of the binding pocket, respectively. In consequence, the hydrophobic contact with the side chain of Trp-116, conserved in FMN, lumichrome, and phloxine B, is absent in erythrosin extra bluish.

Contrary to FMN and lumichrome, phloxine B and erythrosin extra bluish establish several additional direct and water-mediated polar interactions with BLVRB. Bromine atoms BR1 and BR2 of phloxine B are almost equidistant (4.3 and 4.0 Å, respectively) to the hydroxyl oxygen of Ser-111. The latter bromine establishes a water-mediated interaction with the side chains of Ser-111 and His-132, whereas bromine BR3 interacts with the carbonyl oxygen of Arg-78. In accordance to its seemingly higher affinity for BLVRB, erythrosin extra bluish displays even more interactions with the enzyme. Unlike the disordered tetrachlorobenzoate moiety of phloxine B, the equivalent benzoate moiety of erythrosin extra bluish is well defined, with its carboxylate group establishing a bidentate interaction with the nicotinamide nitrogen of $NADP^+$ and the side chain of His-153, in addition to water-mediated contacts with the carbonyl oxygen of Ile-154, the side chain nitrogen of Gln-14, the side chain oxygen of Asn-79, and the $NADP^+$ pyrophosphate. Additionally, the four iodine substituents of erythrosin extra bluish engage in direct or solvent-mediated interactions. Iodine atom I establishes a bond with the hydroxyl of Thr-77, as well as water-mediated contacts with the main chain nitrogen of Asn-79, and the pyrophosphate group and the nicotinamide nitrogen of $NADP^+$. Atoms I1 and I2 establish water-mediated bonds with the carbonyl oxygen of Arg-174 and erythrosin oxygen O4, respectively. Finally, I3 is within direct bonding distance of the hydroxyl group of Ser-111, and establishes solvent-mediated contacts with the side chains of Ser-111, Thr-129, and His-132.

Cellular effects of BLVRB inhibitors

In vitro effects of BLVRB inhibitors were subsequently studied in promyelocytic HL-60 cells, using resazurin reduction as a live probe of BLVRB functional redox activity. HL-60 cells express endogenous BLVRB, although overexpression caused time-dependent enhancement of redox activity compared with mock-transfected controls (Fig. 6, *a* and *b*). Exaggerated redox coupling was not due to cellular expansion (Fig. 6*c*), establish-

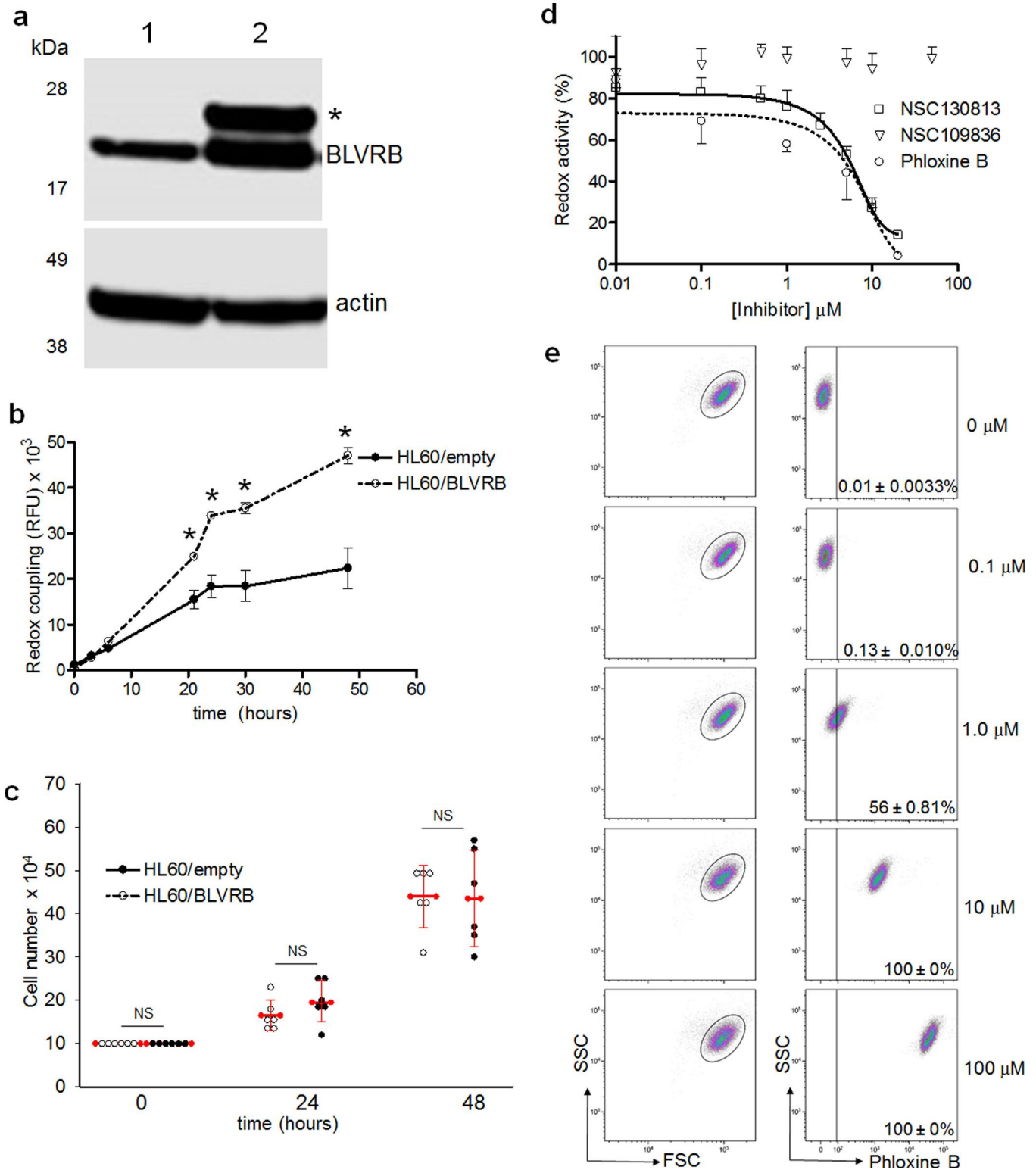

Figure 6. Cellular effects of BLVRB inhibitors. *a,* immunoblot of control or HL-60/BLVRB cells (15 μg/lane). Exogenous (His and V5-tagged) BLVRB is delineated by the *asterisk* (*). *b* and *c,* cells (1×10^5/well) were plated and propagated for specified times for determination of resazurin-based redox coupling (*panel B*) or cell counts using trypan blue exclusion (*panel C*). Data in *panel B* are presented as mean ± S.E. from triplicate wells from a representative experiment repeated once; *, *p* value <0.05. Data in *panel C* are presented as individual counts with the mean ± S.D.; *NS,* not significant. *d,* HL-60/BLVRB cells (1×10^4/well) were incubated for 24 h with various concentrations of BLVRB inhibitors (phloxine B or NSC130813) or control NSC109836 for determination of redox activity; data presented as mean ± S.E. from triplicate wells from a single experiment repeated on two occasions. Redox activity is expressed as percentage relative to the solvent only (no inhibitor) control. *e,* HL-60/BLVRB cells (1×10^5/well) were incubated for 24 h with various concentrations of phloxine B, at which point cells were harvested for flow cytometric quantification (Ex_{540}/Em_{564}). The gated populations at each concentration (*FSC*, forward scatter, *versus SSC*, side scatter), along with intracellular phloxine B accumulation are shown. *Numbers* in each scatter grid represent percent cellular positivity (mean ± S.E., $n = 3$); progressive dose-dependent increase in geometric ($\log_{10}$) fluorescent mean (phloxine B accumulation) is evident.

ing the BLVRB-dependent nature of the resazurin coupling reaction. Incubation of HL-60/BLVRB cells with either xanthene (phloxine B)- or acridine (NSC130813)-based BLVRB inhibitors caused dose-dependent loss of redox activity with no inhibitory effects using the modest BLVRB inhibitor NSC109836 (Fig. 6*d*, refer to Table S1). The cellular EC_{50} of both compounds was comparable (5.2 ± 1 μM (NSC130813) and 3.1 ± 1 μM (phloxine B)) despite their distinct biochemical properties (Table 1), presumably explained by differential cellular bioavailability or target binding affinities. For phloxine B, we exploited its fluorescence properties to validate a direct relationship between intracellular accumulation and cellular redox activity. As shown, flow cytometric quantification confirmed a clear dose-dependent increase in cellular uptake and intracellular phloxine B accumulation as quantified by the geometric fluorescent mean intensity (Fig. 6*e*). Phloxine B at a concentration (10 μM) resulting in >99% cellular uptake resulted in ~70% cellular redox inhibition, with nearly complete inhibition evident with progressive intracellular accumulation (100 μM). These results confirm that biochemical inhibition has selective effects on BLVRB-dependent intracellular redox coupling.

Discussion

We have used both *in silico* and crystallographic studies to identify and characterize BLVRB small molecule inhibitors retaining potencies nearly ~400 times greater than the previously described inhibitor lumichrome (22). The most potent inhibitors contain a tricyclic hydrocarbon core structure that is similar to the isoalloxazine ring of the BLVRB substrate FMN and to the alloxazine ring of lumichrome. Acridine-based compounds were computationally located within the substrate-binding site adjacent to the nicotinamide moiety of the $NADP^+$ cofactor and predicted to bind primarily through hydrophobic interactions with BLVRB. Attempts to obtain an experimental structure of the BLVRB–$NADP^+$–NSC130813 complex have been hampered by the low aqueous solubility of the ligand, although crystal structures of the xanthene-based inhibitors erythrosin extra bluish and phloxine B were solvable. Structures were nearly identical to ligand-free BLVRB (22), with ligands found within the ample BLVRB-binding site adjacent to the nicotinamide moiety of the cofactor and bordered by the flexible loops 80, 120, and the N-terminal half of the helix αE (27). Although erythrosin extra bluish and phloxine B bind less deeply than FMN or lumichrome into the BLVRB active site, both compounds interact with the side chain of Ser-111, a residue previously identified as critical for maintenance of the enzymatic active site (27) and cellular reductase functions that maintain redox balance and antioxidant handling in hematopoietic cells (26). Consistent with what is observed in the crystal structures for phloxine B- and erythrosin-bound BLVRB, the halogen located on the tricyclic hydrocarbon of NSC130813 and NSC12516 is predicted to be in close proximity to Ser-111 (Fig. 2, *a* and *b*). Although the precise mechanism(s) by which these compounds inhibit BLVRB remains under investigation, this common protein–ligand interaction highlights critical requirements for enzymatic activity.

Kinetic studies using our top BLVRB inhibitors resulted in double-reciprocal plots that indicated non-competitive inhibition against FMN, although it is clear from crystallographic studies that phloxine B and erythrosin extra bluish occupy the same binding site as the substrate. These findings contrast what was observed for lumichrome, a competitive inhibitor with respect to FMN with a K_i of 76 μM (17). The discrepancy between our crystallographic and kinetic experiments may indicate a complex mode of inhibition for these inhibitors (*e.g.* tight binding (33)). Additionally, results reported herein indicate that enzyme–inhibitor interactions between BLVRB and erythrosin extra bluish and phloxine B display Goldstein's zone B behavior (34, 35) *versus* the zone A behavior that is observed for lumichrome.

Enzymatic assays confirm inhibitory effects using two distinct BLVRB substrates, FMN and DCPIP. Because both verdins and flavins bind within the single Rossmann-fold, we characterized inhibition of biliverdin reductase activity using a BV isomeric mixture generated by coupled oxidation from a heme– heme oxygenase (HemO) complex previously known to selectively generate BVIXβ and BVIXδ (36), both of which serve as substrates for BLVRB (37). In contrast to what was observed when FMN and DCPIP were used as substrates, we did not observe a significant inhibition of biliverdin reductase activity in the presence of our inhibitors at concentrations suitable for inhibition of flavin reductase and DCPIP reductase activities (10 μM phloxine B and erythrosin extra bluish and 200 μM NSC130813). This is not unexpected given the known technical limitations arising from the use of tetrapyrrole substrates, which variably demonstrate inhibition (at low concentrations) or activation (at higher doses) of BLVRB's biliverdin reductase activity dependent on the nature of the tetrapyrrole (37, 38). Indeed protohemin, a compound that inhibits BLVRB's flavin reductase activity, was shown to activate the enzyme's biliverdin reductase activity (16). Additionally, lumichrome (a well-characterized inhibitor of BLVRB's flavin reductase activity) does not inhibit the biliverdin reductase activity of the enzyme (16). These observations highlight the technical difficulties associated with characterizing BLVRB's biliverdin reductase activity, although flavin inhibitory effects remain evident.

The most potent acridine derivative (NSC130813) is predicted to have the greatest affinity and specificity for BLVRB based on our computational models, although previous functions as a topoisomerase inhibitor (39), a ligand for bacterial RNA (40) and inhibitor of ERCC1–XPF protein–protein interactions (41) have been described. This is not unexpected given the known cancer-modulatory characteristics of the starting NCI Diversity Set used for the initial *in silico* screen. In contrast, erythrosin extra bluish and phloxine B have less well-characterized functions, although effects on protein–protein interactions within the tumor necrosis superfamily have been delineated (42). Interestingly, both phloxine B and erythrosin extra bluish display inhibitor effects on uridine 5′-diphospate (UDP) glucuronosyltransferase 1A6 (UGT1A6) (43, 44), the enzyme responsible for bilirubin glucuronidation and hereditary unconjugated hyperbilirubinemic disorders (Gilbert's and Crigler-Najjar syndromes) (45). Detailed biochemical mechanism(s) of this effect are not well established, and direct enzymatic inhibition with structural interactions as outlined here have not been described.

Of the two classes of inhibitors identified in this study, the acridine-based compounds possess the most drug-like properties (*i.e.* molecular weight, octanol-water partition coefficient (logP), hydrogen bond donors/acceptors, etc.) (Fig. S2). Based on a BOILED-Egg analysis of the acridine-based compounds, there is high probability that NSC130813 and NSC12516 will passively cross the blood-brain barrier (BBB) (Fig. S3). In contrast, PH006888 and PH001924 are not predicted to cross the BBB. All four acridine-based compounds are predicted to be highly absorbed by the gastrointestinal tract. Although the drug-like properties of phloxine B and erythrosin extra bluish are inferior to the acridine-based compounds, xanthene-based compounds have been shown to have promising therapeutic indications (46, 47).

BLVRB induction (nearly 40-fold) has been identified during terminal erythropoiesis (26), and BLVRB overexpression has been identified in multiple tumor subtypes, including but not limited to cervical cancer, hepatocellular carcinoma, and triple-negative breast cancer (Protein-Atlas, proteinatlas.org/ENSG00000090013-BLVRB/pathology),[5] furthermore, targeted BLVRB down-regulation suppresses hepatocellular carcinoma cell growth (49). Unlike BLVRA whose pleiotropic cellular effects are mediated by multidomain features (50), the BLVRB structure is generally featureless with a function presumably limited to its substrate/NAD(P)H redox activity (22). Indeed, BLVRB inhibition caused selective loss of redox coupling *in vitro*, suggesting that these compounds can now be used to address target validity and further refine differences in substrate utilization relevant to various human models linked to hematopoiesis and/or cancer proliferation. Ongoing studies designed to characterize *BLVRB-null* cells and *BLVRB* knockout mice will provide further insight into target selectivity and physiological role(s) of this enzyme in development and redox-regulated cellular functions.

The identification of first-generation BLVRB inhibitors may now be applied to better dissect the role of biliverdins, alternative substrates, and BLVRB expression in hematopoietic and cancer subtypes. Indeed, the recent development of phytochrome-optimized infrared probes retaining distinct biliverdin-dependent red shifted fluorescence (59) document that cells accumulate biliverdins. Although there are limited data on BV quantification (and/or isomeric distribution) across cell types, the availability of these and optimized structure-based inhibitory compounds provide a critical framework for further dissection of BLVRB cellular effects.

Experimental procedures

Materials

FMN, NADPH, DCPIP, biliverdin, HEPES, PH002274, PH002289, PH006888, PH001924, NSC130813, lumichrome, phloxine B, erythrosin extra bluish, xanthene, proflavine, safranin O, and Alizarin Red S were purchased from Sigma. Cayman Chemical Company and Santa Cruz Biotechnology served as secondary sources for phloxine B and erythrosin extra bluish, respectively. NSC compounds were obtained from the National Cancer Institute Developmental Therapeutic Program Repository. Commercially available ZINC compounds were purchased from ChemDiv with the exception of ZINC4366439 (NSC12516), which was obtained from the Developmental Therapeutic Program Repository.

Protein expression and purification

Recombinant BLVRB was overexpressed and purified as a glutathione *S*-transferase (GST) fusion protein in BL21(DE3) cells as previously described (51). Briefly, protein expression was induced using 0.1 mM isopropyl β-D-1-thiogalactopyranoside and allowed to proceed for 3 h at 37 °C. GST-tagged BLVRB was purified by affinity chromatography using glutathione-Sepharose 4B, and the fusion protein was cleaved overnight at 4 °C with 1 nM thrombin to remove the GST tag, and purified BLVRB lacking the GST tag was eluted from the column with phosphate-buffered saline (PBS). BLVRB concentration was determined using the bicinchoninic acid assay (52) with BSA as the standard.

Enzymatic activity assays

Inhibition assays were performed using a Synergy H1 hybrid microplate reader (BioTek). Flavin reductase activity was determined spectrophotometrically by monitoring the rate of oxidation of NADPH to $NADP^+$ at 340 nm ($\epsilon = 6200\ M^{-1}\ cm^{-1}$). Enzymatic activity was measured at 25 °C in 100 mM HEPES, pH 7.0, containing 200 μM FMN, 100 μM NADPH, and 200 μM inhibitor (except where noted). Dye-based inhibitors were assayed at a final concentration of 10 μM. Reactions were initiated by the addition of 450 nM enzyme. Assays lacking inhibitor (solvent only) and enzyme served as positive and negative controls, respectively. Secondary inhibition assays were run using DCPIP (50 μM) as the substrate in a reaction containing 100 mM HEPES, pH 7.0, and 100 μM NADPH at 25 °C. Reactions were initiated by the addition of 100 nM BLVRB and reductase activity was measured by following the decrease in absorbance at 600 nm corresponding to the reduction of DCPIP ($\epsilon = 20.7\ mM^{-1}\ cm^{-1}$) (53).

The concentration of inhibitor required to inhibit enzymatic activity by 50% (IC_{50}) was determined by adding varying concentrations of inhibitor to reaction mixtures at fixed concentrations of substrate FMN (200 μM) or DCPIP (50 μM) and NADPH (100 μM). The total amount of organic solvent added was kept constant at a final concentration of 2% (v/v). IC_{50} values were determined by non-liner regression fits of data to Equation 1 using GraFit 4.0 (Erithacus Software),

$$y = \frac{100\%}{1 + \left(\frac{[I]}{IC_{50}}\right)^s} \quad \text{(Eq. 1)}$$

where y is the percent activity, $[I]$ is the concentration of inhibitor, and s is the slope factor. Controls lacking enzyme were run at each concentration of inhibitor to determine any background caused by the inhibitor.

The mode of inhibition was determined by varying the concentration of inhibitor at fixed concentrations of FMN (25, 50,

[5] Please note that the JBC is not responsible for the long-term archiving and maintenance of this site or any other third party hosted site.

100, 150, and 200 μM) and a fixed concentration of 100 μM NADPH in 100 mM HEPES, pH 7.0, at 25 °C. Reactions were initiated by the addition of 360 nM BLVRB with the exception 600 nM BLVRB being used for NSC130813 experiments. Lineweaver-Burk plots were generated from transformed data using the program SigmaPlot 12.5 (Systat Software Inc.) and inhibition constants were determined by fitting data to standard equations for competitive and non-competitive inhibition (Equations 2 and 3, respectively),

$$V = \frac{V_{max}[S]}{K_M\left(1 + \frac{[I]}{K_i}\right) + [S]} \quad \text{(Eq. 2)}$$

$$V = \frac{V_{max}[S]}{K_M\left(1 + \frac{[I]}{K_i}\right) + [S]\left(1 + \frac{[I]}{K_i}\right)} \quad \text{(Eq. 3)}$$

where V_{max} is the maximal velocity, [S] is the substrate concentration, K_M is the Michaelis-Menten constant for the substrate, $[I]$ is the concentration of inhibitor added to the reaction, and K_i is the inhibition constant.

BLVRA assays were performed in the scanning kinetics mode (800–320 nm) using a Cary 60 UV-visible spectrophotometer. Reactions were run in 50 mM Tris-HCl, pH 8.7, containing 100 μM NADPH and 10 μM biliverdin at 37 °C. Reactions were initiated by the addition of 50 ng of enzyme (Fitzgerald, 30R-137) and enzymatic activity was monitored following the conversion of biliverdin (ϵ_{650nm} = 14.3 mM^{-1} cm^{-1}) (37) to bilirubin (ϵ_{450nm} = 53 mM^{-1} cm^{-1}) (37). BLVRB biliverdin reductase assays were performed as described for BLVRA with the following modifications: reactions were run in 100 mM HEPES, pH 7.0, containing 100 μM NADPH, 37 μM bovine serum albumin, and 10 μM biliverdin (IXδ/IXβ). Reactions were initiated by the addition of 200 nM BLVRB. Reductase activity was monitored following the conversion of biliverdin (ϵ_{650nm} = 15.4 mM^{-1} cm^{-1}) (37) to bilirubin (ϵ_{450nm} = 20.5 mM^{-1} cm^{-1}) (37).

Ligand docking validation

All docking experiments were carried out using AutoDock 4.26 (54) unless otherwise noted. Molecular docking was carried out to predict binding modes of compounds to BLVRB. Docking experiments were validated by docking lumichrome into the ligand-binding site of the BLVRB–$NADP^+$–lumichrome X-ray crystal structure (PDB entry 1HE5 (22)). A r.m.s. deviation of ≤2 Å of docked poses relative to the X-ray crystal structure ligand pose was used as the threshold for determining docking success. Calculations obtained from docking lumichrome into the ligand-binding pocket of BLVRB were used to determine the docking parameters for inhibitors.

Two-dimensional virtual screening

A 2D-VS was performed by targeting the ligand-binding site of BLVRB against the Developmental Therapeutics Program NCI Diversity Set IV database. $NADP^+$ as a cofactor was present within the binding site (other ligands and water were deleted) and side chains of residues and termini protons were assigned according to their corresponding protonation state at pH 7.0. Molecular docking calculations were run to explore the conformation space of ligands for further ISR calculations. ISR was calculated using Equation 4,

$$ISR = \frac{\delta E}{\Delta E\sqrt{2S}} \quad \text{(Eq. 4)}$$

where δE is the energy gap, ΔE is the energy roughness, and the size of the binding funnel measured by the entropy S.

Docking simulations were carried out using a grid size of 80 × 80 × 80 and spacing of 0.375 Å, with respect to the binding pocket of BLVRB, and grid maps for scoring were created using AutoGrid. Dockings (10,000 runs) were performed using the AutoDock score function for evaluation and the Lamarckian Genetic Algorithm (LGA) for sampling poses. Molecular modeling was carried out using default parameters with the following exceptions: population size of 100 and the energy evaluation of 100,000 per run with the maximum number of generations of 27,000. Docking results were evaluated according to predicted binding affinities and the subsequent cluster analysis was based on a r.m.s. deviation cutoff of 2.0 Å.

Similar compound library preparation

Compounds structurally similar to the hit compound NSC130813 were identified using five complementary approaches. The first approach employed a similarity search against the ZINC database (55) using a Tanimoto score of 0.8 as the threshold for compound selection. The 123 compounds identified from this screen were further filtered by 3D atom pair fingerprint (3D-APfp) (56) with a Max Count set to 50 to identify compounds with 3D molecular shape similar to NSC130813 and the top 50 hits were selected as potential inhibitors of BLVRB. Second, a LigCSRre similarity search (57) was run using NSC130813 as the query to identify compounds within the program's 13 ligand databases that have maximum common substructure similarity to NSC130813 based on the CSR algorithm. This search resulted in the identification of 400 potential BLVRB inhibitors with a minimal r.m.s. deviation of 1.0 Å. Third, a SHApe-FeaTure Similarity (SHAFTS) search (58) was run against the ZINC database (30). This hybrid 3D (rigid superposition) similarity calculation method integrates pharmacophore match and shape similarity. Using a similarity score of 0.8, 15,900 compounds were identified as potential inhibitors of BLVRB. The fourth approach, Multi-Fingerprint browser for ZINC (MCSS) (59), was utilized to rapidly identify close analogs of NSC130813 in the ZINC database (30). The use of MCSS' four fingerprints, sFP (substructure fingerprint), ECFP4 (extended connectivity fingerprint), MQN (Molecular Quantum Numbers), and SMIfp (SMILES fingerprint), allowed for the identification of 2,477 compounds that were determined to be nearest neighbors of NSC130813 based on city-block distance. The Max Count was set to 500 for this screen. Last, a pharmacophore similarity search against the ZINC database (30) using ZINCPharmer (60) was performed resulting in 932 similar compounds that were further filtered by 3D extended atom pair fingerprint (3D-Xfp) (56), using a minimal r.m.s. deviation of 1.0 Å, to identify the top 50 compounds.

Analysis of inhibitor binding mode

Interactions between BLVRB and inhibitors were initially established based on AutoDock scores. Docking modes for top hits were further evaluated using knowledge-based DSX pair potentials derived from the DrugScore (61, 62) available from DSX^{online} (63). Analyses for binding modes obtained from molecular docking and the detailed contribution (per-atom scores) of each interaction were displayed in PyMOL. Two-dimensional schematic representations of predicted interactions between inhibitors and residues within the binding site of BLVRB were generated using Ligplot+ (64).

Drug-likeness filtering and ADME prediction

Potential inhibitors of BLVRB were filtered to determine their absorption, distribution, metabolism, excretion, and toxicity (ADME/Tox) and drug-likeness properties using FAF-Drugs3 (65) and Molsoft[5] program, respectively. Detailed ADME/Tox profiles of validated hit compounds were evaluated using SwissADME (66). This program allowed for *in silico* prediction of key ADME parameters including gastrointestinal absorption, BBB permeation, cytochrome P450 inhibition, and whether these hits served as substrates for P-glycoprotein. Ligand efficiencies (LE) for top hits were determined using Equation 5,

$$LE = 1.4(-\log IC_{50})/N \quad \text{(Eq. 5)}$$

where IC_{50} is the concentration of inhibitor required to inhibit the enzyme by 50% and N is the number of non-hydrogen bonds. Compounds within the similar compounds library that were drug-like and had acceptable (predicted) ADME/Tox properties were subjected to two-dimensional virtual screening as described above.

Oral toxicity analysis

Rodent oral toxicities of hit compounds were predicted *in silico* using ProTox (67). The median oral lethal dose (LD_{50}) of hit compounds was determined based on known toxicities of structurally related compounds.

Crystallization of BLVRB

Recombinant human BLVRB was crystallized as previously described (22). The phloxine B and erythrosin extra bluish complexes were prepared by soaking the BLVRB–NADP crystals in mother liquor containing 50 mM ligand for 24 h at 20 °C. The crystals of the resulting ternary complexes were cryoprotected by brief (~5 s) sequential transfers to mother liquor supplemented with increasing concentrations (up to 15% (v/v)) of glycerol, plunged in liquid nitrogen, and stored under cryogenic conditions until measured.

Data collection and processing

X-ray diffraction data were collected from single, cryocooled (100 K) crystals at beamline ID23-1 (68) of the European Synchrotron Radiation Facility (ESRF, Grenoble, France). For each complex, a low-resolution pass with 1 degree rotation and 0.1-s exposure per image, and a high-resolution pass with 0.5 degree rotation and 0.1-s exposure per image were collected, using radiation of 0.9763-Å wavelength. The low-resolution pass was composed of 140 or 200 images and the high-resolution pass comprised 300 or 400 images, for the phloxine B or the erythrosin extra bluish complex crystal, respectively.

The data were processed with XDS (69), scaled with AIMLESS (70), and reduced with utilities from the CCP4 suite (71). The data collection and processing statistics are summarized in Table S4. The diffraction data (http://dx.doi.org/10.15785/SBGRID/484, http://dx.doi.org/10.15785/SBGRID/485, http://dx.doi.org/10.15785/SBGRID/486, http://dx.doi.org/10.15785/SBGRID/487) were deposited with the SBGrid Data Bank (72).

Structure determination and refinement

The structure of ternary BLVRB complexes were solved by molecular replacement with PHASER (73) using the coordinates of BLVRB (PDB entry 1HDO (22)) stripped from ligands and solvent as search model. To reduce model bias, the protein moiety was automatically rebuilt using ARP/wARP (74) and the resulting models were subjected to alternating cycles of manual building with COOT (75) and refinement with PHENIX (76) until model completion. The refinement statistics are summarized in Table S5. All crystallographic software was supported by SBGrid (77). The refined three-dimensional coordinates and structure factors were deposited at the Protein Data Bank with accession codes 5OOG (phloxine B) and 5OOH (erythrosin extra bluish).

Analysis of atomic structures

Superposition of atomic structures was performed with the program Theseus (78). The molecular structures shown in Figs. 4 and 5 were depicted with PyMOL, version 1.6.0 (Schrödinger).

Cell-based assays

Promyelocytic HL-60 cells (ATCC CCL-240) were maintained as suspension cultures in Iscove's modified Dulbecco's medium supplemented with 20% FBS. Stable BLVRB-expressing cell lines HL-60/BLVRB were generated by lentivirus (Lv) infection (or empty control) using multiplicity of infection of 5, followed by puromycin (2 μg/ml) selection as previously described (26); Lv/BLVRB was expressed with chimeric C-terminal His_6 and V5 tags (79) to distinguish endogenous from exogenous proteins. Uninfected cells (*i.e.* virus-deficient) supplemented with puromcycin demonstrated complete cell death by 24 h. Cellular oxidation/reduction activity was quantified *in vitro* using the NADPH-dependent redox coupler resazurin; cells (1×10^4/well) were plated and propagated in complete medium with various concentrations (or not) of inhibitor compounds, followed by addition of resazurin (0.1% (v/v)) for fluorimetric detection of reduced resorufin ($Ex_{530\ nm}/Em_{590\ nm}$); cellular counts were quantified in parallel using trypan blue exclusion on an automated cell counter (Countess, Thermo Fisher Scientific).

Intracellular accumulation of phloxine B was quantified using a BD LSR Fortessa flow cytometer (BD Biosciences) as previously described (48, 80, 81). HL-60 cells (1×10^5/well) were plated overnight, followed by incubation with various concentrations (or not) of phloxine B for 24 h, at which point

cells were harvested, washed twice with PBS, and passed through a cell strainer for flow cytometric analyses. Unstained cells were used for definition of background gates, followed by data acquisition of 20,000 gated events using logarithmic gain settings for light scatter and phloxine B ($Ex_{540\ nm}/Em_{564\ nm}$) fluorescence detection (26, 81). Flow cytometric data were exported and analyzed using Kaluza software (Beckman Coulter).

Immunoblotting analysis

BLVRB expression in HL-60 cells was determined from exponentially growing cells, harvested for lysate preparation using sonication in RIPA buffer (10 mM Tris-HCl, pH 8.0, 1 mM EDTA, 0.5 mM EGTA, 1% (v/v) Triton X-100, 0.1% (w/v) sodium deoxycholate, 0.1% (w/v) SDS, 140 mM NaCl). Protein lysates were size-fractionated by SDS-PAGE as previously described (26), and immunodetection was completed using a 1:200 dilution of sheep anti-human BLVRB antibody (R&D Systems, AF6568), followed by 1:10,000 dilution of donkey anti-sheep antibody (Jackson ImmunoResearch, 713-035-147); or a 1:1,000 dilution of mouse anti-actin antibody (Thermo Fisher Scientific, MA1-744) followed by a 1:10,000 dilution of anti-mouse antibody (GE Healthcare, NA93107); protein detection was completed by enhanced chemiluminescence using a Luminata™ Forte Western HRP substrate and visualized using a LI-COR C-DiGit® blot scanner.

Statistics

All statistical comparisons were established using unpaired *t* test, defining $p < 0.05$ for statistical significance.

Author contributions—N. M. N., X. Z., P. J. B. P., T. J. M., J. W., and W. F. B. conceptualization; N. M. N., X. Z., J. A. M., W.-Y. Y., L. E. M., J. R.-R., P. J. B. P., J. W., and W. F. B. data curation; N. M. N., X. Z., J. A. M., W.-Y. Y., L. E. M., J. R.-R., P. J. B. P., T. J. M., J. W., and W. F. B. formal analysis; N. M. N., X. Z., J. A. M., J. R.-R., P. J. B. P., J. W., and W. F. B. funding acquisition; N. M. N., X. Z., Z. L., J. A. M., W.-Y. Y., L. E. M., J. R.-R., P. J. B. P., J. W., and W. F. B. investigation; N. M. N., X. Z., Z. L., J. A. M., W.-Y. Y., L. E. M., J.R.-R., P. J. B. P., T. J. M., J. W., and W. F. B. methodology; N. M. N. and X. Z. writing-original draft; N. M. N., J. W., and W. F. B. project administration; N. M. N., X. Z., J. A. M., P. J. B. P., T. J. M., J. W., and W. F. B. writing-review and editing; X. Z., P. J. B. P., and J. W. software; P. J. B. P., J. W., and W. F. B. resources; P. J. B. P., J. W., and W. F. B. supervision.

Acknowledgments—We acknowledge the ESRF (European Synchrotron Radiation Facility) for provision of synchrotron radiation facilities and thank the ESRF staff for help with data collection.

References

1. Gozzelino, R., Jeney, V., and Soares, M. P. (2010) Mechanisms of cell protection by heme oxygenase-1. *Annu. Rev. Pharmacol. Toxicol.* **50,** 323–354 CrossRef Medline
2. Abraham, N. G., and Kappas, A. (2008) Pharmacological and clinical aspects of heme oxygenase. *Pharmacol. Rev.* **60,** 79–127 CrossRef Medline
3. Stocker, R., Yamamoto, Y., McDonagh, A. F., Glazer, A. N., and Ames, B. N. (1987) Bilirubin is an antioxidant of possible physiological importance. *Science* **235,** 1043–1046 CrossRef Medline
4. Bulmer, A. C., Blanchfield, J. T., Toth, I., Fassett, R. G., and Coombes, J. S. (2008) Improved resistance to serum oxidation in Gilbert's syndrome: a mechanism for cardiovascular protection. *Atherosclerosis* **199,** 390–396 CrossRef Medline
5. Vítek, L., Jirsa, M., Brodanová, M., Kalab, M., Marecek, Z., Danzig, V., Novotný, L., and Kotal, P. (2002) Gilbert syndrome and ischemic heart disease: a protective effect of elevated bilirubin levels. *Atherosclerosis* **160,** 449–456 CrossRef Medline
6. Schwertner, H. A., Jackson, W. G., and Tolan, G. (1994) Association of low serum concentration of bilirubin with increased risk of coronary artery disease. *Clin. Chem.* **40,** 18–23 Medline
7. Baranano, D. E., Rao, M., Ferris, C. D., and Snyder, S. H. (2002) Biliverdin reductase: a major physiologic cytoprotectant. *Proc. Natl. Acad. Sci. U.S.A.* **99,** 16093–16098 CrossRef Medline
8. Yamaguchi, T., and Nakajima, H. (1995) Changes in the composition of bilirubin-IX isomers during human prenatal development. *Eur. J. Biochem.* **233,** 467–472 CrossRef Medline
9. Kavanagh, K. L., Jornvall, H., Persson, B., and Oppermann, U. (2008) Medium- and short-chain dehydrogenase/reductase gene and protein families: the SDR superfamily: functional and structural diversity within a family of metabolic and regulatory enzymes. *Cell Mol. Life Sci.* **65,** 3895–3906 CrossRef
10. Noguchi, M., Yoshida, T., and Kikuchi, G. (1979) Purification and properties of biliverdin reductases from pig spleen and rat liver. *J. Biochem.* **86,** 833–848 CrossRef Medline
11. Kutty, R. K., and Maines, M. D. (1981) Purification and characterization of biliverdin reductase from rat liver. *J. Biol. Chem.* **256,** 3956–3962 Medline
12. Schluchter, W. M., and Glazer, A. N. (1997) Characterization of cyanobacterial biliverdin reductase: conversion of biliverdin to bilirubin is important for normal phycobiliprotein biosynthesis. *J. Biol. Chem.* **272,** 13562–13569 CrossRef Medline
13. Kikuchi, A., Park, S. Y., Miyatake, H., Sun, D., Sato, M., Yoshida, T., and Shiro, Y. (2001) Crystal structure of rat biliverdin reductase. *Nat. Struct. Biol.* **8,** 221–225 CrossRef Medline
14. Shalloe, F., Elliott, G., Ennis, O., and Mantle, T. J. (1996) Evidence that biliverdin-IXβ reductase and flavin reductase are identical. *Biochem. J.* **316,** 385–387 CrossRef Medline
15. Mack, C. P., Hultquist, D. E., and Shlafer, M. (1995) Myocardial flavin reductase and riboflavin: a potential role in decreasing reoxygenation injury. *Biochem. Biophys. Res. Commun.* **212,** 35–40 CrossRef Medline
16. Cunningham, O., Dunne, A., Sabido, P., Lightner, D., and Mantle, T. J. (2000) Studies on the specificity of the tetrapyrrole substrate for human biliverdin-IXα reductase and biliverdin-IXβ reductase: structure-activity relationships define models for both active sites. *J. Biol. Chem.* **275,** 19009–19017 CrossRef Medline
17. Cunningham, O., Gore, M. G., and Mantle, T. J. (2000) Initial-rate kinetics of the flavin reductase reaction catalyzed by human biliverdin-IXβ reductase (BVR-B). *Biochem. J.* **345,** 393–399 Medline
18. Xu, F., Mack, C. P., Quandt, K. S., Shlafer, M., Massey, V., and Hultquist, D. E. (1993) Pyrroloquinoline quinone acts with flavin reductase to reduce ferryl myoglobin *in vitro* and protects isolated heart from re-oxygenation injury. *Biochem. Biophys. Res. Commun.* **193,** 434–439 CrossRef Medline
19. Smith, L. J., Browne, S., Mulholland, A. J., and Mantle, T. J. (2008) Computational and experimental studies on the catalytic mechanism of biliverdin-IXβ reductase. *Biochem. J.* **411,** 475–484 CrossRef Medline
20. McDonagh, A. F. (2001) Turning green to gold. *Nat. Struct. Biol.* **8,** 198–200 CrossRef Medline
21. Fu, G., Liu, H., and Doerksen, R. J. (2012) Molecular modeling to provide insight into the substrate binding and catalytic mechanism of human biliverdin-IXα reductase. *J. Phys. Chem. B* **116,** 9580–9594 CrossRef Medline
22. Pereira, P. J., Macedo-Ribeiro, S., Párraga, A., Perez-Luque, R., Cunningham, O., Darcy, K., Mantle, T. J., and Coll, M. (2001) Structure of human biliverdin IXβ reductase, an early fetal bilirubin IXβ producing enzyme. *Nat. Struct. Biol.* **8,** 215–220 CrossRef Medline
23. Mitchell, A. E., Jones, A. D., Mercer, R. S., and Rucker, R. B. (1999) Characterization of pyrroloquinoline quinone amino acid derivatives by electrospray ionization mass spectrometry and detection in human milk. *Anal. Biochem.* **269,** 317–325 CrossRef Medline
24. Kumazawa, T., Seno, H., Urakami, T., Matsumoto, T., and Suzuki, O. (1992) Trace levels of pyrroloquinoline quinone in human and rat samples

detected by gas chromatography/mass spectrometry. *Biochim. Biophys. Acta* **1156,** 62–66 CrossRef Medline
25. Hultquist, D. E., Xu, F., Quandt, K. S., Shlafer, M., Mack, C. P., Till, G. O., Seekamp, A., Betz, A. L., and Ennis, S. R. (1993) Evidence that NADPH-dependent methemoglobin reductase and administered riboflavin protect tissues from oxidative injury. *Am. J. Hematol.* **42,** 13–18 CrossRef Medline
26. Wu, S., Li, Z., Gnatenko, D. V., Zhang, B., Zhao, L., Malone, L. E., Markova, N., Mantle, T. J., Nesbitt, N. M., and Bahou, W. F. (2016) BLVRB redox mutation defines heme degradation in a metabolic pathway of enhanced thrombopoiesis in humans. *Blood* **128,** 699–709 CrossRef Medline
27. Chu, W. T., Nesbitt, N. M., Gnatenko, D. V., Li, Z., Zhang, B., Seeliger, M. A., Browne, S., Mantle, T. J., Bahou, W. F., and Wang, J. (2017) Enzymatic activity and thermodynamic stability of biliverdin IXβ reductase are maintained by an active site serine. *Chem. Eur. J.* **23,** 1891–1900 CrossRef Medline
28. Yubisui, T., Matsuki, T., Takeshita, M., and Yoneyama, Y. (1979) Characterization of the purified NADPH-flavin reductase of human erythrocytes. *J. Biochem.* **85,** 719–728 Medline
29. Wang, J., Zheng, X., Yang, Y., Drueckhammer, D., Yang, W., Verkhivker, G., and Wang, E. (2007) Quantifying intrinsic specificity: a potential complement to affinity in drug screening. *Phys. Rev. Lett.* **99,** 198101 CrossRef
30. Irwin, J. J., and Shoichet, B. K. (2005) ZINC: a free database of commercially available compounds for virtual screening. *J. Chem. Inf. Model* **45,** 177–182 CrossRef Medline
31. Lipinski, C. A., Lombardo, F., Dominy, B. W., and Feeney, P. J. (2001) Experimental and computational approaches to estimate solubility and permeability in drug discovery and development settings. *Adv. Drug Deliv. Rev.* **46,** 3–26 CrossRef Medline
32. Morris, G. M., Huey, R., Lindstrom, W., Sanner, M. F., Belew, R. K., Goodsell, D. S., and Olson, A. J. (2009) AutoDock4 and AutoDockTools4: automated docking with selective receptor flexibility. *J. Comput. Chem.* **30,** 2785–2791 CrossRef Medline
33. Copeland, R. A. (2000) *Enzymes: A practical introduction to structure, mechanism, and data analysis*, Second Ed., Wiley-VCH, New York
34. Straus, O. H., Goldstein, A., and Technical Assistance of Frank, L. P. (1943) Zone behavior of enzymes: illustrated by the effect of dissociation constant and dilution on the system cholinesterase-physostigmine. *J. Gen Phys.* **26,** 559–585 CrossRef
35. Goldstein, A. (1944) The mechanism of enzyme-inhibitor-substrate reactions: illustrated by the cholinesterase-physostigmine-acetylcholine system. *J. Gen. Phys.* **27,** 529–580 CrossRef
36. Barker, K. D., Barkovits, K., and Wilks, A. (2012) Metabolic flux of extracellular heme uptake in *Pseudomonas aeruginosa* is driven by the iron-regulated heme oxygenase (HemO). *J. Biol. Chem.* **287,** 18342–18350 CrossRef Medline
37. Yamaguchi, T., Komoda, Y., and Nakajima, H. (1994) Biliverdin-IX alpha reductase and biliverdin-IXβ reductase from human liver: purification and characterization. *J. Biol. Chem.* **269,** 24343–24348 Medline
38. Franklin, E. M., Browne, S., Horan, A. M., Inomata, K., Hammam, M. A., Kinoshita, H., Lamparter, T., Golfis, G., and Mantle, T. J. (2009) The use of synthetic linear tetrapyrroles to probe the verdin sites of human biliverdin-IXα reductase and human biliverdin-IXβ reductase. *FEBS J.* **276,** 4405–4413 CrossRef Medline
39. Stivers, J., and Kwon, K. (January 24, 2008) Assays for identification of topoisomerase inhibitors. U. S. Patent 20080020973A1
40. Yan, Z., Sikri, S., Beveridge, D. L., and Baranger, A. M. (2007) Identification of an aminoacridine derivative that binds to RNA tetraloops. *J. Med. Chem.* **50,** 4096–4104 CrossRef Medline
41. Jordheim, L. P., Barakat, K. H., Heinrich-Balard, L., Matera, E. L., Cros-Perrial, E., Bouledrak, K., El Sabeh, R., Perez-Pineiro, R., Wishart, D. S., Cohen, R., Tuszynski, J., and Dumontet, C. (2013) Small molecule inhibitors of ERCC1-XPF protein-protein interaction synergize alkylating agents in cancer cells. *Mol. Pharmacol.* **84,** 12–24 CrossRef Medline
42. Ganesan, L., Margolles-Clark, E., Song, Y., and Buchwald, P. (2011) The food colorant erythrosine is a promiscuous protein-protein interaction inhibitor. *Biochem. Pharmacol* **81,** 810–818 CrossRef Medline
43. Uesugi, N., Furumiya, K., and Mizutani, T. (2006) Inhibition mechanism of UDP-glucuronosyltransferase 1A6 by xanthene food dyes. *J. Health Sci.* **52,** 549–557 CrossRef
44. Mizutani, T. (2009) Toxicity of xanthene food dyes by inhibition of human drug-metabolizing enzymes in a noncompetitive manner. *J. Environ Public Health* **2009,** 1–9 CrossRef
45. Peters, W. H., te Morsche, R. H., and Roelofs, H. M. (2003) Combined polymorphisms in UDP-glucuronosyltransferases 1A1 and 1A6: implications for patients with Gilbert's syndrome. *J. Hepatol.* **38,** 3–8 Medline
46. Cai, Z., and Sheppard, D. N. (2002) Phloxine B interacts with the cystic fibrosis transmembrane conductance regulator at multiple sites to modulate channel activity. *J. Biol. Chem.* **277,** 19546–19553 CrossRef Medline
47. Wong, H. E., Irwin, J. A., and Kwon, I. (2013) Halogenation generates effective modulators of amyloid-β aggregation and neurotoxicity. *PloS One* **8,** e57288 CrossRef Medline
48. Gnatenko, D. V., Dunn, J. J., McCorkle, S. R., Weissmann, D., Perrotta, P. L., and Bahou, W. F. (2003) Transcript profiling of human platelets using microarray and serial analysis of gene expression. *Blood* **101,** 2285–2293 CrossRef Medline
49. Huan, L., Bao, C., Chen, D., Li, Y., Lian, J., Ding, J., Huang, S., Liang, L., and He, X. (2016) MicroRNA-127–5p targets the biliverdin reductase B/nuclear factor-κB pathway to suppress cell growth in hepatocellular carcinoma cells. *Cancer Sci.* **107,** 258–266 CrossRef Medline
50. Kapitulnik, J., and Maines, M. D. (2009) Pleiotropic functions of biliverdin reductase: cellular signaling and generation of cytoprotective and cytotoxic bilirubin. *Trends Pharmacol. Sci.* **30,** 129–137 CrossRef Medline
51. Cunningham, O., and Mantle, T. J. (1997) Cloning, overexpression and purification of biliverdin IX-β reductase. *Biochem. Soc. Trans.* **25,** S613 CrossRef Medline
52. Smith, P. K., Krohn, R. I., Hermanson, G. T., Mallia, A. K., Gartner, F. H., Provenzano, M. D., Fujimoto, E. K., Goeke, N. M., Olson, B. J., and Klenk, D. C. (1985) Measurement of protein using bicinchoninic acid. *Anal. Biochem.* **150,** 76–85 CrossRef Medline
53. Hägerhall, C., Aasa, R., von Wachenfeldt, C., and Hederstedt, L. (1992) Two hemes in *Bacillus subtilis* succinate:menaquinone oxidoreductase (complex II). *Biochemistry* **31,** 7411–7421 CrossRef Medline
54. Morris, G. M., Goodsell, D. S., Halliday, R. S., Huey, R., Hart, W. E., Belew, R. K., and Olson, A. J. (1998) Automated docking using a Lamarckian genetic algorithm and an empirical binding free energy function. *J. Comput Chem.* **19,** 1639–1662 CrossRef
55. Irwin, J. J., Sterling, T., Mysinger, M. M., Bolstad, E. S., and Coleman, R. G. (2012) ZINC: a free tool to discover chemistry for biology. *J. Chem. Inf. Model* **52,** 1757–1768 CrossRef Medline
56. Awale, M., Jin, X., and Reymond, J. L. (2015) Stereoselective virtual screening of the ZINC database using atom pair 3D-fingerprints. *J. J. Cheminform.* **7,** 3 CrossRef
57. Quintus, F., Sperandio, O., Grynberg, J., Petitjean, M., and Tuffery, P. (2009) Ligand scaffold hopping combining 3D maximal substructure search and molecular similarity. *BMC Bioinformatics* **10,** 245 CrossRef Medline
58. Liu, X., Jiang, H., and Li, H. (2011) SHAFTS: A hybrid approach for 3D molecular similarity calculation: 1. method and assessment of virtual screening. *J. Chem. Inf. Model* **51,** 2372–2385 CrossRef Medline
59. Awale, M., and Reymond, J. L. (2014) A multi-fingerprint browser for the ZINC database. *Nucleic Acids Res.* **42** W234–W239
60. Koes, D. R., and Camacho, C. J. (2012) ZINCPharmer: pharmacophore search of the ZINC database. *Nucleic Acids Res.* **40,** W409–W414 CrossRef Medline
61. Meng, E. C., Shoichet, B. K., and Kuntz, I. D. (1992) Automated docking with grid-based energy evaluation. *J. Comput. Chem.* **13,** 505–524 CrossRef
62. Velec, H. F., Gohlke, H., and Klebe, G. (2005) DrugScore^{CSD} knowledge-based scoring Function derived from small molecule crystal data with superior recognition rate of near-native ligand poses and better affinity prediction. *J. Med. Chem.* **48,** 6296–6303 CrossRef Medline
63. Neudert, G., and Klebe, G. (2011) DSX: A knowledge-based scoring function for the assessment of protein-ligand complexes. *J. Chem. Inf. Model* **51,** 2731–2745 CrossRef Medline

64. Laskowski, R. A., and Swindells, M. B. (2011) LigPlot+: multiple ligand-protein interaction diagrams for drug discovery. *J. Chem. Inf. Model* **51,** 2778–2786 CrossRef
65. Lagorce, D., Sperandio, O., Baell, J. B., Miteva, M. A., and Villoutreix, B. O. (2015) FAF-Drugs3: a web server for compound property calculation and chemical library design. *Nucleic Acids Res.* **43,** W200–W207 CrossRef Medline
66. Daina, A., Michielin, O., and Zoete, V. (2017) SwissADME: A free web tool to evaluate pharmacokinetics, drug-likeness and medicinal chemistry friendliness of small molecules. *Sci. Rep.* **7,** 42717 CrossRef Medline
67. Drwal, M. N., Banerjee, P., Dunkel, M., Wettig, M. R., and Preissner, R. (2014) ProTox: a web server for the *in silico* prediction of rodent oral toxicity. *Nucleic Acids Res.* **42,** W53–W58 CrossRef Medline
68. Nurizzo, D., Mairs, T., Guijarro, M., Rey, V., Meyer, J., Fajardo, P., Chavanne, J., Biasci, J. C., McSweeney, S., and Mitchell, E. (2006) The ID23–1 structural biology beamline at the ESRF. *J. Synchrotron Radiat.* **13,** 227–238 CrossRef Medline
69. Kabsch, W. (2010) Integration, scaling, space-group assignment and post-refinement. *Acta Crystallogr. D Biol. Crystallogr.* **66,** 133–144 CrossRef Medline
70. Evans, P. R. (2011) An introduction to data reduction: Space-group determination, scaling and intensity statistics. *Acta Crystallogr. D Biol. Crystallogr.* **67,** 282–292 CrossRef Medline
71. Winn, M. D., Ballard, C. C., Cowtan, K. D., Dodson, E. J., Emsley, P., Evans, P. R., Keegan, R. M., Krissinel, E. B., Leslie, A. G., McCoy, A., McNicholas, S. J., Murshudov, G. N., Pannu, N. S., Potterton, E. A., Powell, H. R., Read, R. J., Vagin, A., and Wilson, K. S. (2011) Overview of the CCP4 suite and current developments. *Acta Crystallogr. D Biol. Crystallogr.* **67,** 235–242 CrossRef Medline
72. Meyer, P. A., Socias, S., Key, J., Ransey, E., Tjon, E. C., Buschiazzo, A., Lei, M., Botka, C., Withrow, J., Neau, D., Rajashankar, K., Anderson, K. S., Baxter, R. H., Blacklow, S. C., Boggon, T. J., *et al.* (2016) Data publication with the structural biology data grid supports live analysis. *Nat. Commun.* **7,** 10882 CrossRef Medline
73. McCoy, A. J., Grosse-Kunstleve, R. W., Adams, P. D., Winn, M. D., Storoni, L. C., and Read, R. J. (2007) Phaser crystallographic software. *J. Appl. Crystallogr.* **40,** 658–674 CrossRef Medline
74. Langer, G., Cohen, S. X., Lamzin, V. S., and Perrakis, A. (2008) Automated macromolecular model building for X-ray crystallography using ARP/wARP version 7. *Nat. Protoc.* **3,** 1171–1179 CrossRef Medline
75. Emsley, P., Lohkamp, B., Scott, W. G., and Cowtan, K. (2010) Features and development of Coot. *Acta Crystallogr. D Biol. Crystallogr.* **66,** 486–501 CrossRef Medline
76. Adams, M. J., Ellis, G. H., Gover, S., Naylor, C. E., and Phillips, C. (1994) Crystallographic study of coenzyme, coenzyme analogue and substrate binding in 6-phosphogluconate dehydrogenase: implications for NADP specificity and the enzyme mechanism. *Structure* **2,** 651–668 CrossRef Medline
77. Morin, A., Eisenbraun, B., Key, J., Sanschagrin, P. C., Timony, M. A., Ottaviano, M., and Sliz, P. (2013) Collaboration gets the most out of software. *eLife* **2,** e01456 Medline
78. Theobald, D. L., and Steindel, P. A. (2012) Optimal simultaneous superpositioning of multiple structures with missing data. *Bioinformatics* **28,** 1972–1979 CrossRef Medline
79. Southern, J. A., Young, D. F., Heaney, F., Baumgärtner, W. K., and Randall, R. E. (1991) Identification of an epitope on the P and V proteins of simian virus 5 that distinguishes between two isolates with different biological characteristics. *J. Gen. Virol.* **72,** 1551–1557 CrossRef Medline
80. Lu, J., Guo, S., Ebert, B. L., Zhang, H., Peng, X., Bosco, J., Pretz, J., Schlanger, R., Wang, J. Y., Mak, R. H., Dombkowski, D. M., Preffer, F. I., Scadden, D. T., and Golub, T. R. (2008) MicroRNA-mediated control of cell fate in megakaryocyte-erythrocyte progenitors. *Dev. Cell* **14,** 843–853 CrossRef Medline
81. Xu, X., Gnatenko, D. V., Ju, J., Hitchcock, I. S., Martin, D. W., Zhu, W., and Bahou, W. F. (2012) Systematic analysis of microRNA fingerprints in thrombocythemic platelets using integrated platforms. *Blood* **120,** 3575–3585 CrossRef Medline